
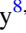






Kepler K2 and TESS Observations of Two Magnetic Cataclysmic Variables: The New Asynchronous Polar SDSS J084617.11+245344.1 and Paloma

Colin Littlefield^{1,2,3} , D. W. Hoard², Peter Garnavich¹ , Paula Szkody² , Paul A. Mason^{4,5} , Simone Scaringi⁶ ,

Krystian Ilkiewicz^{6,7} , Mark R. Kennedy^{8,9} , Saul A. Rappaport¹⁰ , and Rahul Jayaraman¹⁰ 

¹ Department of Physics and Astronomy, University of Notre Dame, Notre Dame, IN 46556, USA; clittlef@alumni.nd.edu

² Department of Astronomy, University of Washington, Seattle, WA 98195, USA

³ Bay Area Environmental Research Institute, Moffett Field, CA 94035 USA

⁴ New Mexico State University, MSC 3DA, Las Cruces, NM, 88003, USA

⁵ Picture Rocks Observatory, 1025 S. Solano Dr., Suite D., Las Cruces, NM 88001, USA

⁶ Centre for Extragalactic Astronomy, Department of Physics, Durham University, South Road, Durham, DH1 3LE, UK

⁷ Astronomical Observatory, University of Warsaw, Al. Ujazdowskie 4, 00-478 Warszawa, Poland

⁸ Department of Physics, University College Cork, Cork, Ireland

⁹ Jodrell Bank Centre for Astrophysics, Department of Physics and Astronomy, The University of Manchester, M19 9PL, UK

¹⁰ Department of Physics and Kavli Institute for Astrophysics and Space Research, MIT, Cambridge, MA 02139, USA

Received 2022 April 11; revised 2022 November 4; accepted 2022 November 7; published 2023 January 9

Abstract

There have been relatively few published long-duration, uninterrupted light curves of magnetic cataclysmic variable stars in which the accreting white dwarf's rotational frequency is slightly desynchronized from the binary orbital frequency. We report Kepler K2 and TESS observations of two such systems. The first, SDSS J084617.11+245344.1, was observed by the Kepler spacecraft for 80 days during Campaign 16 of the K2 mission, and we identify it as a new asynchronous polar with a likely 4.64 hr orbital period. This is significantly longer than any other asynchronous polar, as well as all but several synchronous polars. Its spin and orbital periods beat against each other to produce a conspicuous 6.77-day beat period, across which the system's accretion geometry gradually changes. The second system in this study, Paloma, was observed by TESS for one sector and was already known to be asynchronous. Until now, there had been an ambiguity in its spin period, but the TESS power spectrum pinpoints a spin period of 2.27 hr. During the resulting 0.7-day spin-orbit beat period, the light curve phased on the spin modulation alternates between being single and double humped. We explore two possible explanations for this behavior: the accretion flow being diverted from one of the poles for part of the beat cycle, or an eclipse of the emitting region responsible for the second hump.

Unified Astronomy Thesaurus concepts: [DQ Herculis stars \(407\)](#); [AM Herculis stars \(32\)](#); [Cataclysmic variable stars \(203\)](#); [White dwarf stars \(1799\)](#)

1. Introduction

1.1. The Three Classes of Magnetic Cataclysmic Variables

Cataclysmic variables (CVs) are interacting binaries in which a white dwarf (WD) accretes from a Roche-lobe-filling companion, usually an M dwarf. If the WD possesses a significant magnetic field, the accretion flow from the donor star will be channeled onto the WD along its magnetic field lines. The accreting matter produces a shock near the WD's surface, and the post-shock material cools by emitting a combination of X-ray bremsstrahlung and optical/near-infrared cyclotron radiation (Cropper 1990).

Magnetic CVs (mCVs) are typically divided into three broad categories—polars, intermediate polars (IPs), and asynchronous polars (APs)—depending on the difference between the spin period (P_{spin}) of the accreting WD and the binary orbital period (P_{orb}). In polars, the WD's magnetic field is strong enough to synchronize P_{spin} to P_{orb} , and no accretion disk forms (for a review, see Cropper 1990). Conversely, if P_{spin} is significantly shorter than P_{orb} , the object is called an IP (Patterson 1994). IPs tend to have accretion disks truncated by

the WD's magnetic field, but if the WD's magnetosphere is large enough, it can prevent a disk from forming.

The third category of mCVs, the APs, is comprised of systems in which P_{spin} and P_{orb} differ by no more than several percent. As Table 1 shows, the current number of APs is anywhere from 7 to 9, depending on how close P_{spin} and P_{orb} are required to be. APs are thought to be polars that have been temporarily desynchronized by nova eruptions. In their study of Nova Cygni 1975 (V1500 Cyg), Stockman et al. (1988) proposed that in the aftermath of the nova, the WD's envelope encompassed the binary, resulting in a coupling between the secondary and WD. When the WD's envelope subsequently shrank, the coupling ceased, which reduced the WD's moment of inertia and caused it to spin up, leaving V1500 Cyg in its current asynchronous state. The short-lived nature of this differential rotation is supported by the observed period-derivative trend toward synchronous rotation in all APs with a sufficiently long observational baseline to detect a change in P_{spin} (e.g., as in V1500 Cyg; Schmidt & Stockman 1991). The key observational distinction between IPs and APs is that in the former, asynchronous rotation is a stable equilibrium (King & Lasota 1991; King 1993; King & Wynn 1999), while in the latter it is not.

Caused by the inequality of P_{spin} and P_{orb} , the differential rotation of the WD produces a number of observable effects in both IPs and APs. The accretion flow in mCVs must become

Table 1
The Asynchronous Polars and Related Systems

Name	P_{orb} (hr)	$P_{\text{spin}}/P_{\text{orb}}$	P_{beat} (days)	Distance (pc)	References
Swift J0503.7–2819	1.36	0.79	0.217	837^{+60}_{-43}	Halpern (2022); Rawat et al. (2022)
		0.89	0.434		Halpern (2022)
IGR J19552+0044	1.39	0.972	2.04	$165.5^{+1.9}_{-1.5}$	Tovmassian et al. (2017)
1RXS J083842.1–282723	1.64	0.96	1.8	$156.0^{+1.9}_{-2.2}$	Halpern et al. (2017)
CD Ind	1.87	0.989	7.3	$235.3^{+4.0}_{-3.2}$	Littlefield et al. (2019)
Paloma	2.62	0.87	0.71	582^{+28}_{-20}	this work
V1500 Cyg	3.351	0.986	9.58	1570^{+270}_{-190}	Pavlenko et al. (2018)
BY Cam	3.354	0.99	15	$264.5^{+1.9}_{-1.7}$	Pavlenko et al. (2013)
V1432 Aql	3.366	1.002	62	450 ± 7	Littlefield et al. (2015)
SDSS J084617.11+245344.1	4.64	0.972	6.77	1230^{+800}_{-290}	this work

Note. The listed distances are the geometric distances computed by Bailer-Jones et al. (2021) from Gaia EDR3 (Gaia Collaboration et al. 2021). Swift J0503.7–2819 is listed twice because at the time of writing, an ambiguity exists in the identification of its beat period and spin-to-orbit ratio. Halpern (2022) reported two possible identifications of the beat period in Swift J0503.7–2819, and an ensuing study by Rawat et al. (2022) argued in favor of the shorter beat period.

magnetically confined at some point after it leaves the secondary, and the relative orientation of the WD’s magnetic field will determine both its path through the magnetosphere and the region where it accretes onto the surface of the WD. In APs and diskless IPs, the magnetosphere rotates with respect to the ballistic accretion stream; this differential rotation causes the stream to gradually plow into different regions of the WD magnetosphere. The stream’s ballistic trajectory is stationary in the binary rest frame, so differential rotation occurs at the spin-orbit beat frequency of $\omega - \Omega$, where $\omega = P_{\text{spin}}^{-1}$ and $\Omega = P_{\text{orb}}^{-1}$, equivalently, $\omega - \Omega$ is the rotational frequency of the WD in the corotating binary rest frame.

The combination of potentially complex magnetic field structures and asynchronism has been modeled magnetohydrodynamically (Zhilkin et al. 2012, 2016), which suggests that pole switching may also accompany changes between one and two accretion pole configurations. However, establishing unique magnetic field configurations from observations remains difficult.

From an observational standpoint, the ever-changing accretion geometry of APs leads to several dramatic effects. For example, the accretion region on the WD will migrate across the WD’s surface, following the footprints of whichever magnetic field lines are capturing the accretion stream at that particular time (Geckeler & Staubert 1997). Likewise, the bulk of the accretion flow will travel to different accretion poles during different portions of the beat cycle, and when the accretion flow switches between poles, the light curve will show a discontinuity in phase (Mason et al. 1989).

1.2. SDSS J084617.11+245344.1

The CV SDSS J084617.11+245344.1 (hereafter J0846) has an exceedingly sparse observational history. Szkody et al. (2006) found that its Sloan Digital Sky Survey (SDSS) spectrum contains unusually prominent He II λ 4686 Å emission, a common indicator of magnetic accretion. The same study was unable to detect circular polarization in a single 6000 s exposure. J0846 is listed in the Catalina Survey Periodic Variable Star Catalog with a period of 0.1827862 days, with no uncertainty specified (Drake et al. 2014).

The Gaia EDR3 (Gaia Collaboration et al. 2016, 2021) distance to J0846 is 1230^{+800}_{-290} pc (Bailer-Jones et al. 2021). Its Galactic latitude of $+35.4^\circ$ therefore places it 710^{+460}_{-170} pc above

the Galactic plane, which is significantly larger than nearly every polar (Beuermann et al. 2021).

1.3. Paloma

The second subject of the present study, Paloma¹¹ (=RX J0524+42), is a rare hybrid between IPs and APs. Schwarz et al. (2007) and Joshi et al. (2016) published in-depth photometric and X-ray studies, respectively, but Paloma has received scant attention otherwise. Schwarz et al. (2007) measured an orbital period of 2.62 hr and constrained the spin period to be either 2.27 hr or 2.43 hr. These differ from the orbital period by 13% and 7%, respectively, so the system could be plausibly classified as either a nearly synchronous IP or a highly asynchronous AP. Schwarz et al. (2007) also discuss the evolutionary implications of the unusual $P_{\text{spin}}/P_{\text{orb}}$ ratio, including the intriguing possibility that it is an IP evolving into a polar, a process envisioned by Channugam & Ray (1984). Power-spectral analysis of the X-ray light curve suggests the absence of an accretion disk (Joshi et al. 2016).

The distance to Paloma based on Gaia EDR3 is 582^{+28}_{-20} pc (Bailer-Jones et al. 2021). Unlike J0846, it is situated very close to the Galactic plane, with a Galactic latitude of $+3^\circ 9'$.

2. Data

2.1. The K2 Observation of J0846

The Kepler spacecraft observed J0846 during Campaign 16 of its K2 mission between 2017 December 7 and 2018 February 25. The observations utilized the long-cadence mode, so the integration time of each datum is 30 minutes.

We extracted the light curve of J0846 using `lightkurve`. To compensate for Kepler’s well-known pointing oscillations, we chose a sufficiently large extraction aperture to encompass the full range of J0846’s drift across the sensor. J0846 is situated in a sparse star field, and its signal does not suffer from serious blending.

¹¹ Although CVs rarely have common names, Paloma (Spanish for “dove”) is an exception. It acquired its name because of its chance superposition next to an unrelated, dove-shaped supernova remnant (Schwarz et al. 2007).

2.2. The TESS Observation of Paloma

The Transiting Exoplanet Survey Satellite (TESS) observed Paloma in its 2-minute-cadence mode during Sector 19, between 2019 November 28 and 2019 December 23. The observations were uninterrupted with the exception of a day-long downlink gap in the middle of the sector. Because of the location of Paloma in a dense star field and the low angular resolution of TESS images, it is heavily blended with nearby sources.

The TESS pipeline creates two versions of each 2-minute-cadence light curve: simple-aperture photometry (SAP) and preconditioned simple-aperture photometry (PDCSAP). The PDCSAP light curve attempts to remove the effects of blending and systematic trends in the data, while the SAP light curve does not. Although this issue has not been addressed authoritatively in the context of CVs, the SAP and PDCSAP fluxes appear to show the same periodic variability, but they can differ significantly with respect to aperiodic variability. For example, the SAP light curve of TX Col and simultaneous ground-based photometry both show an outburst, while the PDCSAP light curve does not (Littlefield et al. 2021; Rawat et al. 2021).

The SAP light curve of Paloma shows a gentle parabolic curvature, while the PDCSAP light curve lacks any overall trend. To determine which light curve to use, we follow the general approach of Hill et al. (2022) and compare both the SAP and PDCSAP light curves against simultaneous r -band photometry from the Zwicky Transient Facility (ZTF; Bellm et al. 2019). We used linear regressions to compare the flux of the seven available ZTF observations with the simultaneous TESS observations and found that the PDCSAP light curve agreed well with the ZTF data, with a coefficient of determination of $r_{\text{PDCSAP}}^2 = 0.54$. In comparison, the SAP light curve initially had $r_{\text{SAP}}^2 = 0.0$, largely because of the influence of a single ZTF measurement that strongly disagreed with the trend in the SAP data. Arbitrarily removing this point resulted in $r_{\text{SAP}}^2 = 0.29$, but there are no obvious indicators that that particular ZTF measurement is unreliable.

Therefore, on the basis of these comparisons, we elected to use the PDCSAP light curve. We stress that unlike TX Col, there are no astrophysically noteworthy differences between the SAP and PDCSAP light curves, so the choice between these two data sets does not significantly impact the results of our analysis. Since a few of the PDCSAP flux measurements are negative, we added an arbitrary constant offset to the PDCSAP flux.

2.3. Paloma Spectra

On 2019 December 19, during the TESS observation of Paloma, we obtained time-resolved spectroscopy with the Large Binocular Telescope (LBT).¹² From 8:06 UT until 10:30 UT, we obtained a series of 180 s exposures with the MODS spectrographs (Pogge et al. 2010), a 250 line mm⁻¹ grating, and a 0''8 slit aligned to the parallactic angle. During

this sequence, the air mass ranged from 1.05 to 1.36. All spectra were flux-calibrated and reduced using IRAF¹³ standard procedures.

The LBT spectra are extremely complex and will be the subject of a dedicated spectroscopic paper. As a result, in this study, we rely upon them sparingly (primarily to establish an orbital ephemeris in order to phase the photometry to the binary orbit).

3. Analysis of the New Asynchronous Polar J0846

3.1. Light Curve

The top panels of Figures 1 and 2 show a representative segment of the K2 light curve of J0846 and its full light curve, respectively. Despite the 30-minute cadence of the observations, it is obvious that J0846 has large-amplitude variability on timescales shorter than the observational cadence. At times, the flux doubles in the span of several hours and is halved in even less time, giving the light curve a jagged appearance. The profiles of individual photometric maxima, with their large amplitudes and rapid changes, are typical for a polar. However, unlike normal polars, both the amplitude and shape of the maxima gradually evolve over a 6.7-day period before returning to their original appearance. This highly periodic and well-defined modulation of the short-term variability is the distinguishing property of J0846's light curve and provides compelling evidence that it is an AP. As we explain in detail in Section 3.2.2, we identify the 6.7-day period in J0846 as the beat between its likely spin ($\omega = 5.32$ cycles day⁻¹) and orbital ($\Omega = 5.17$ cycles day⁻¹) frequencies.

The changes in the light curve across the beat period result in a rich power spectrum (Figure 1, middle and bottom panels) containing ω , Ω , and numerous sidebands and harmonics thereof. The time-resolved power spectrum (Figure 2) shows that the power spectrum varies cyclically at the beat period. Here again, this behavior is expected in an AP and has been observed in TESS observations of the AP CD Ind (Hakala et al. 2019; Littlefield et al. 2019; Mason et al. 2020).

Our classification of J0846 as an AP is supported by the previously reported observations of the system. As we noted earlier, an SDSS spectrum obtained in 2004 and published in Szkody et al. (2006) was consistent with J0846 being a polar. Figure 3, which averages the previously reported SDSS spectrum with two additional spectra obtained in 2018 and 2019, confirms that He II $\lambda 4686$ Å is of comparable strength to H β and that the emission lines are single peaked, properties that are commonly observed in polars.¹⁴ Although Szkody et al. (2006) did not detect circular polarization in a single 6000 s interval, this time span covered significantly less than half of one cycle of the photometric variations in Figures 1 and 2. Inopportune sampling could therefore explain the absence of circular polarization in that observation.

¹² The LBT is an international collaboration among institutions in the United States, Italy, and Germany. LBT Corporation partners are the University of Arizona on behalf of the Arizona university system; Istituto Nazionale di Astrofisica, Italy; LBT Beteiligungsgesellschaft, Germany, representing the Max-Planck Society, the Astrophysical Institute Potsdam, and Heidelberg University; The Ohio State University; and The Research Corporation, on behalf of The University of Notre Dame, University of Minnesota, and University of Virginia.

¹³ IRAF is distributed by the National Optical Astronomy Observatory, which is operated by the Association of Universities for Research in Astronomy (AURA) under a cooperative agreement with the National Science Foundation.

¹⁴ To improve legibility, the individual spectra are not shown in Figure 3, but except for changes in the strength of the He I emission, the three spectra were largely similar.

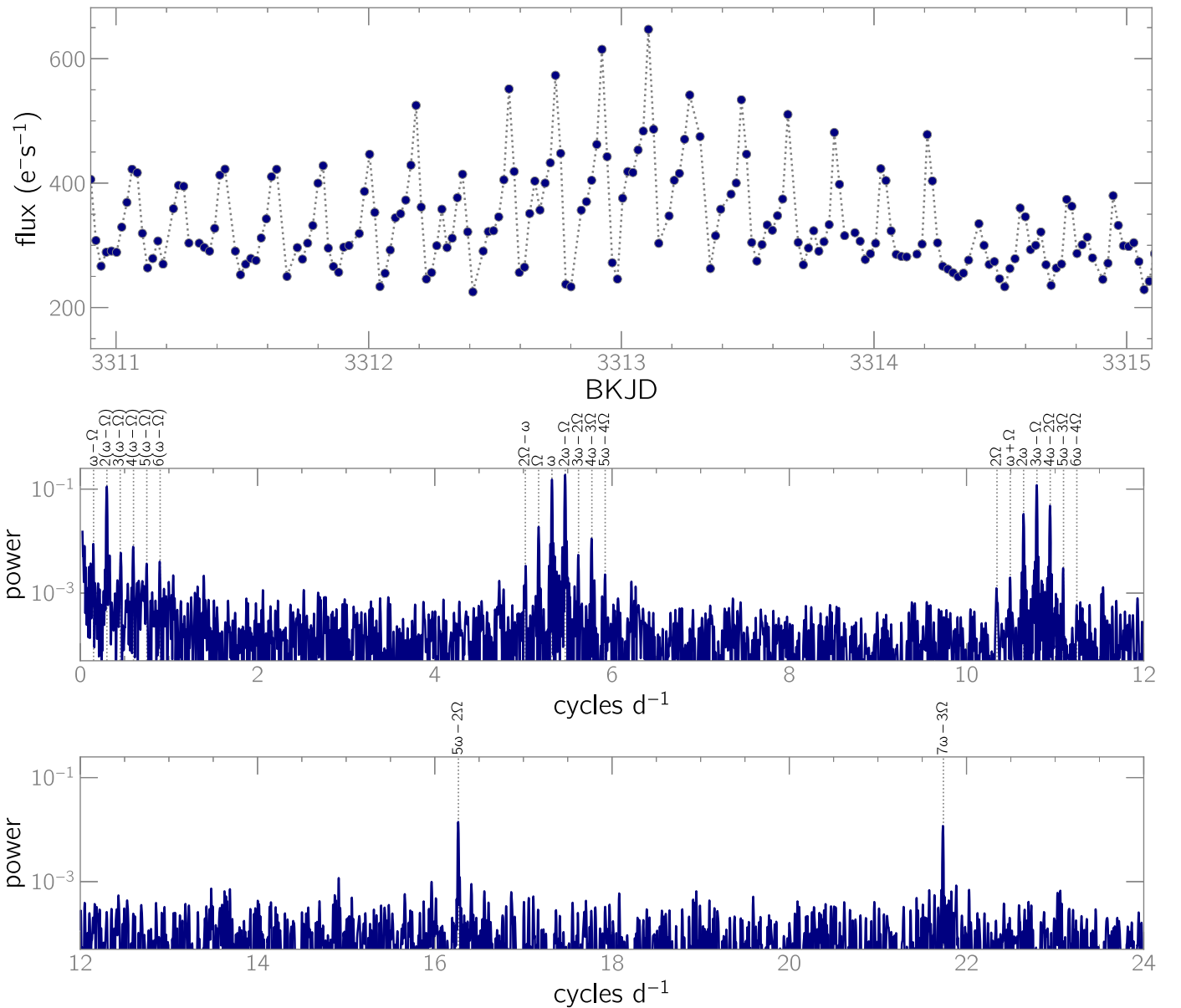


Figure 1. Top panel: representative ~ 4 -day segment of the K2 light curve of J0846. Each datum is a 30-minute integration, and consecutive measurements have been joined with dotted line segments to guide the eye. Flux uncertainties are negligibly small at this scale. BKJD is defined as $\text{JD} - 2,454,833$. Middle and bottom panels: Lomb–Scargle power spectrum of the K2 light curve of J0846, split into two panels to improve the visibility of major frequencies. ω is the WD’s spin frequency and Ω is the binary orbital frequency.

3.2. Interpreting J0846’s Power Spectrum

3.2.1. Theoretical Considerations for AP Power Spectra

Even with a long, uninterrupted light curve, the identification of the spin and orbital frequencies in APs is fraught with difficulties not otherwise encountered in the study of CVs.

With synchronous polars, the accretion region is expected to be stationary at a fixed mass-transfer rate, so for purposes of measuring the WD’s spin period, it is often treated as a fiducial marker of the star’s rotation. In APs, however, the accretion region moves across the surface of the WD and even jumps between magnetic poles, making the photometric modulation of the accretion region an unreliable indicator of the spin period.

Indeed, by causing large phase shifts in the light curve, the movement of the accretion region wreaks havoc on the power

spectrum. Wynn & King (1992) predicted that in X-ray light curves of IPs pole switching could cause the dominant frequency in the power spectrum to be $2\omega - \Omega$, even if the light curve is modulated at ω between the pole switches (Mason et al. 2020). The widely used Lomb–Scargle periodogram (Lomb 1976; Scargle 1982), along with other common period-finding algorithms, presumes that a signal does not experience these large, regular phase jumps, and if pole switching is present in a light curve, these algorithms will be biased toward the identification of a period that forces a signal to remain in-phase as possible (Section 4.1 in Littlefield et al. 2019).

Mason et al. (1995) and Mason et al. (1998) extended the rationale of Wynn & King (1992) to optical observations of APs and identified the $2\omega - \Omega$ sideband as the strongest signal in the power spectrum of BY Cam. In a similar vein, Littlefield et al. (2019) concluded from the TESS light curve of CD Ind

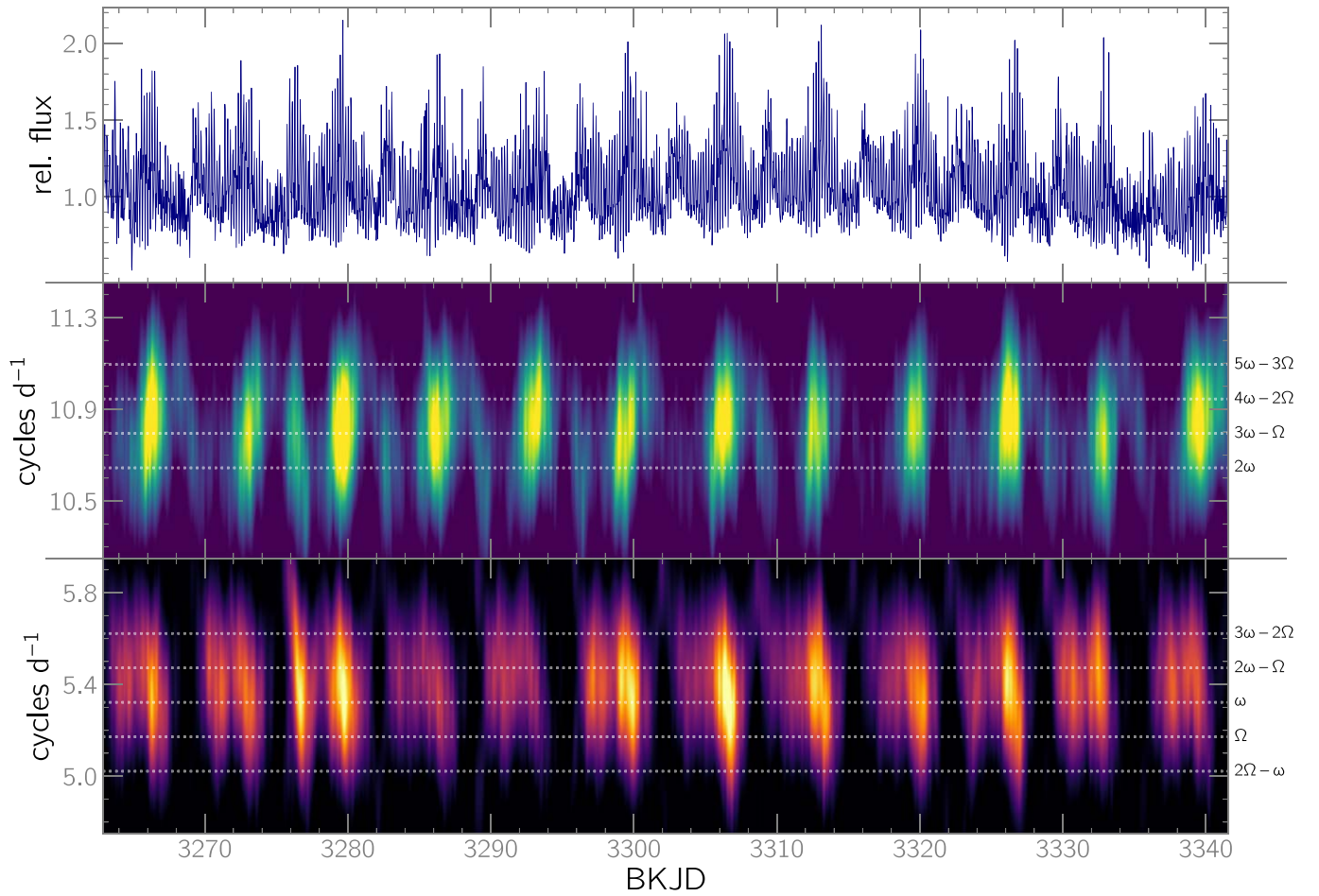


Figure 2. Light curve and 2D power spectra for J0846. BKJD is defined as BJD $-2,454,833$. The middle and bottom panels use different color maps to reflect that they have different intensity cuts. The size of the sliding window is 0.5 days.

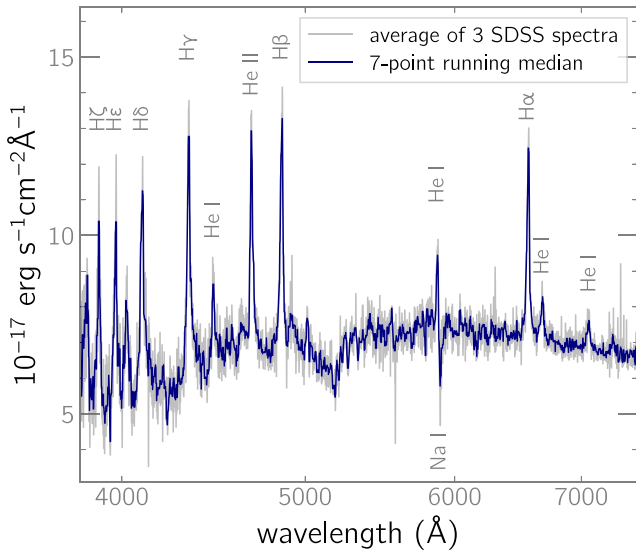


Figure 3. Average of three SDSS spectra of J0846, including one obtained during the K2 observation, showing very strong He II $\lambda 4686$ emission and single-peaked emission lines. Both are commonly observed features in spectra of polars. Overall, this spectrum is similar to the one reported in Szkody et al. (2006), except that He I emission is more pronounced here. The absorption feature near 5200 Å is attributable to MgH from the secondary. As discussed in Section 3.5, we estimate the secondary’s spectral type to be between K5 and M0, with K7 being the most likely classification.

that the long-accepted identification of the spin frequency in that system is actually $2\omega - \Omega$ (although this proposal awaits independent spectroscopic confirmation).

There is yet another complication: even between pole switches, the accretion region is expected to move longitudinally across the surface of the WD (Geckeler & Staubert 1997). The asynchronous rotation of the WD, with respect to the binary, causes the accretion stream to thread onto a continuously changing ensemble of magnetic field lines, each of which channels material onto different points along the WD’s surface. Consequently, in an AP, the interval between the accretion region’s crossings of the WD’s meridian can differ by several percent from the true WD rotational period (Geckeler & Staubert 1997).

Although accurately identifying ω and Ω from photometry alone is therefore a challenging affair, it is comparatively easy to identify their beat frequency ($\omega - \Omega$). Even if $\omega - \Omega$ is not directly visible in the power spectrum, it will be observable as the spacing between sideband frequencies of ω and Ω .

3.2.2. Frequency Identifications in J0846

With these considerations in mind, we turn to the power spectrum of J0846 and examine two sets of possible frequency identifications in the observed power spectrum of J0846.

The unusually rich power spectrum of J0846 (middle and bottom panels of Figure 1) bears many similarities to the TESS power spectrum of CD Ind and is consistent with J0846 being

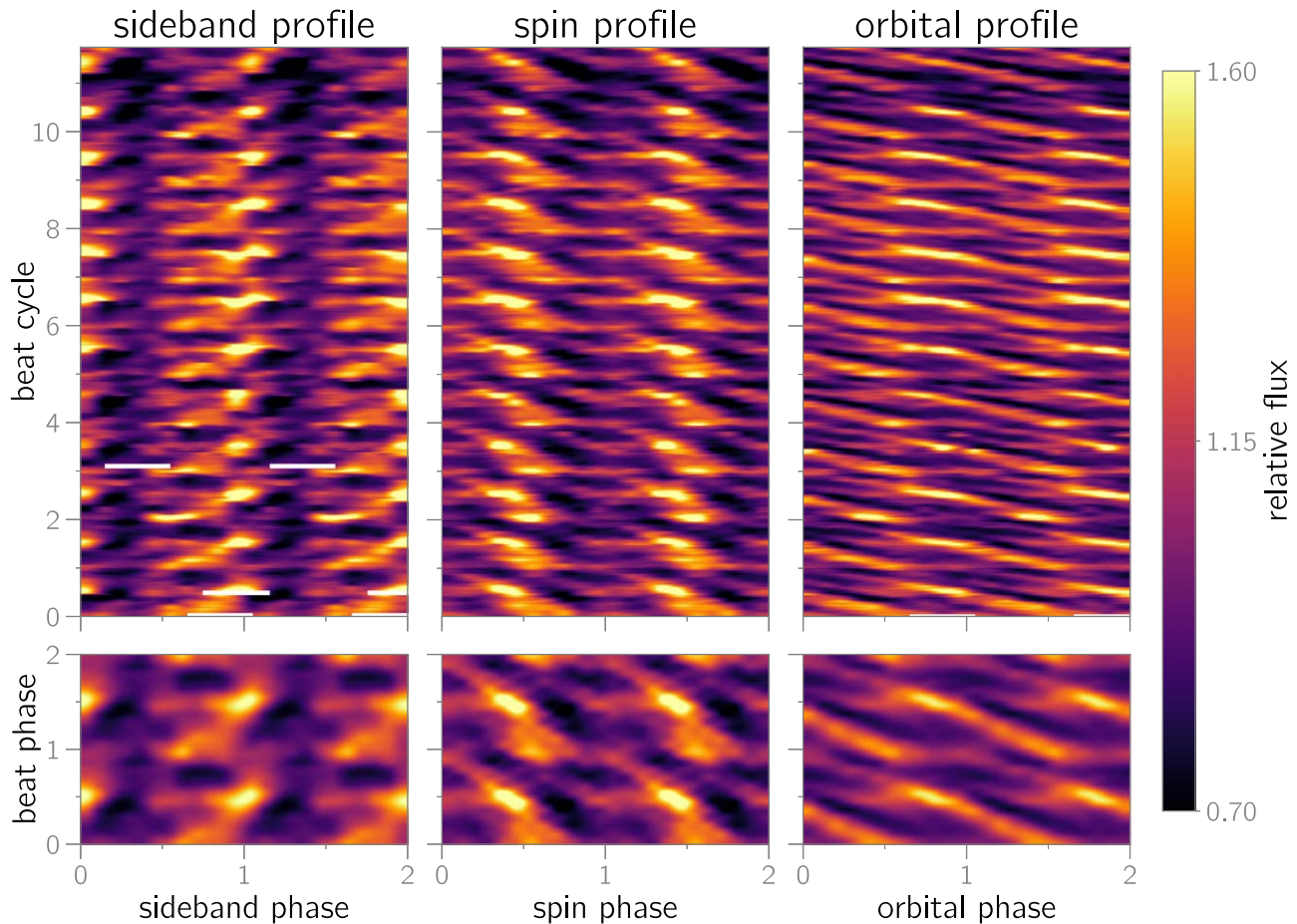


Figure 4. 2D light curves of J0846 phased to the sideband, spin, and orbital periods. Phase 0.0 is arbitrary in all panels.

an AP. The major signals in the power spectrum are clustered in three groups, and the signal with the most power occurs at a frequency of $5.47 \text{ cycles day}^{-1}$. This is the same frequency measured by the Drake et al. (2014) pipeline from survey photometry. Nearby at $5.32 \text{ cycles day}^{-1}$ is another major signal. At lower frequencies, there is a family of six harmonically related signals, with the fundamental being $0.15 \text{ cycles day}^{-1}$; this is also the spacing between the frequencies in the other two clusters of signals.

The power spectrum is amenable to two sets of frequency identifications, and while both agree that the beat frequency ($\omega - \Omega$) is $0.15 \text{ cycles day}^{-1}$, they diverge on the correct identifications of ω and Ω . Following Mason et al. (1995) and Mason et al. (1998), we propose that the highest-amplitude signal ($5.47 \text{ cycles day}^{-1}$) is the $2\omega - \Omega$ sideband. In this scenario, which we shall refer to as Case 1, $P_{\text{spin}} = 5.32 \text{ cycles day}^{-1}$ and $P_{\text{orb}} = 5.17 \text{ cycles day}^{-1}$. The phased light curves based on the Case 1 identifications are presented in Figure 4. The $2\omega - \Omega$ sideband profile shows the behavior qualitatively explained by Littlefield et al. (2019) for CD Ind; when phased to this frequency, the pulses remain comparatively in-phase throughout the observation. Littlefield et al. (2019) contended that this is due to a bias of frequency-analysis algorithms. The spin-phased profiles, conversely, show evidence of discrete, variable accretion regions on opposite sides of the WD.

There is an additional set of plausible frequency identifications in which the dominant signal in the power spectrum

Table 2
J0846 Frequency Identifications

Frequency	Case 1	Case 2
Ω	$5.17 \text{ cycles day}^{-1}$	$5.32 \text{ cycles day}^{-1}$
ω	$5.32 \text{ cycles day}^{-1}$	$5.47 \text{ cycles day}^{-1}$
$2\omega - \Omega$	$5.47 \text{ cycles day}^{-1}$	$5.62 \text{ cycles day}^{-1}$

Note. We argue in favor of Case 1, but Case 2 is possible.

would be the spin frequency, such that $\omega = 5.47 \text{ cycles day}^{-1}$. In this scenario, which we call Case 2, $\Omega = 5.32 \text{ cycles day}^{-1}$. Returning to the phased light curves in Figure 4, the nominal sideband-phased and spin-phased light curves from Case 1 would actually be the spin-phased and orbit-phased light curves, respectively, in Case 2.

We summarize both sets of frequency identifications in Table 2. While we favor Case 1, the proper identification of the orbital period can be conclusively ascertained with time-series spectroscopy of the secondary. An undisputed orbital period, in combination with the 6.7-day beat period, would also eliminate any remaining ambiguity surrounding the spin period.

In either set of frequency identifications, J0846 would have an unusually long orbital period for a polar. At the time of writing, the International Variable Star Index (VSX) catalog

contains 146 confirmed or candidate polars;¹⁵ if the orbital period of J0846 is 4.64 hr, as we have argued, only three systems (V895 Cen, V1309 Ori, and V479 And) would have longer orbital periods. That census would increase to only four polars (with AI Tri being the fourth) if J0846’s orbital period is instead 4.51 hr, as it would be in the second, disfavored set of frequency identifications.

3.3. Accretion Geometry

Assuming that Case 1 correctly identifies the spin period, the profile of the spin pulse across the beat cycle is extremely intricate. The spin profile often resembles that of a synchronous polar across short intervals of the beat cycle, particularly during beat phases 0.0–0.25 (where $T_{0,\text{beat}}$ is arbitrarily defined as $\text{BJD} = 2,458,095.4882$). During the next quarter of the beat cycle, the profile develops a plateau, while its peak becomes sharp and narrow, with a conspicuous dip after the pulse maximum. For much of the remainder of the beat cycle, the pulse profile becomes comparatively ill-defined, particularly at beat phase 0.8. Nevertheless, the main accretion region appears to be active for well over half of the beat cycle.

These behaviors are difficult to reconcile with a centered, dipolar field. Such a configuration would be expected to result in diametrically opposed accretion regions on opposite sides of the WD, with each pole accreting during opposite halves of the beat cycle. There is very clearly a dominant accretion region near spin phase 0.5, but there is also a signal near spin phase 1.0 at two different points in the beat cycle. Due to the 30-minute cadence of the observations, we cannot confidently discern whether this is a second accretion spot or simply an evolution of the photometric profile of the main accretion spot. The latter might occur as a result of the migration of the accretion region in both longitude and latitude across the beat cycle, as first described by Geckeler & Staubert (1997) in a different AP, V1432 Aql.

Pole switching in J0846 is much less pronounced than it is in the first TESS observation of CD Ind (Hakala et al. 2019; Littlefield et al. 2019; Mason et al. 2020). In the CD Ind light curve, there was a conspicuous jump in phase, as well as a change in the pulse profile, whenever the accretion flow switched between magnetic poles (Littlefield et al. 2019). In J0846, the pulse profile of the main accretion region experiences obvious changes, but it never switches off in the same manner as CD Ind. However, the poor phase resolution of the K2 light curve means that any single rotational cycle is sampled fewer than 10 times, whereas CD Ind’s spin profile was much more favorably sampled by TESS.

3.4. Comparing J0846 to Other APs

J0846 is the seventh mCV for which the condition $P_{\text{spin}}/P_{\text{orb}} \gtrsim 0.96$ holds true, and it has by far the longest orbital period of the systems listed in Table 1. Two additional mCVs in Table 1 are significantly more asynchronous, making it unclear whether they are best classified as APs or alternatively as extreme IPs. The first of those systems, Paloma, has $P_{\text{spin}}/P_{\text{orb}} = 0.87$, based on our analysis in Section 4, as well as the studies by Schwarz et al. (2007)

and, in particular, Joshi et al. (2016). The other system, Swift J0503.7–2819, currently suffers from an ambiguity in the identification of its spin and beat periods, leading to a $P_{\text{spin}}/P_{\text{orb}}$ ratio of either 0.79 or 0.89 (Halpern 2022); however, Rawat et al. (2022) argue in favor of the former.

Of the known APs, V1432 Aql is a clear outlier, based on its very small level of asynchronism, its eclipsing nature, and the fact that it alone has $P_{\text{spin}} > P_{\text{orb}}$. On that final point, however, Wang et al. (2020) used a new power-spectral modeling technique to propose new identifications of the orbital frequencies of CD Ind and BY Cam, and they argued that $P_{\text{spin}} > P_{\text{orb}}$ in these two systems too.¹⁶ The Wang et al. (2020) proposal can be tested conclusively by measuring P_{orb} from the radial-velocity variations of the donor star in each system; unlike the complex photometric variations, the orbital motion of the secondary must, by definition, occur at P_{orb} .

3.5. Spectral Classification

The secondary star in J0846 contributes significantly to the SDSS spectrum in Figure 3, imprinting an obvious MgH feature but no noticeable VO or TiO absorption bands. To estimate its spectral type, we used χ^2 minimization to model the continuum as the sum of a grid of template SDSS spectra (Bochanski et al. 2007) and a blackbody curve to represent the secondary star and the WD/accretion luminosity, respectively. For each combination of a template spectrum and a blackbody, the scaling factors for both the template and the blackbody were allowed to vary freely, as was the blackbody temperature. Although cyclotron emission can strongly deviate from a blackbody curve, the spectrum in Figure 3 does not show any discernible cyclotron humps, suggesting that the use of a blackbody curve is acceptable.

Based on this approach, we estimate the secondary’s spectral type to be K7, but given the relatively modest signal-to-noise ratio in the continuum, our fits suggest that it could be as early as K5 or as late as M0. Due to the relatively modest signal-to-noise ratio, the fitting was not sensitive to the metallicity of the secondary.

The relative ease of detecting the secondary’s absorption features means that a future study will be able to unambiguously identify the orbital frequency, offering a straightforward opportunity to decisively test our photometric frequency identifications.

4. Paloma

4.1. Frequency Identifications

Paloma is a faint and blended source in the TESS data, but its complex variability is visible in Figure 5. The sliding-window size of 6 hr in the 2D power spectrum in the middle panel of Figure 5 captures the cyclical transfer of power between ω and 2ω across the 0.7-day beat cycle.

The power spectrum for the full data set (Figure 6) provides an opportunity to resolve the long-standing ambiguity concerning the correct identification of the spin period. Schwarz et al. (2007) proposed and carefully justified two possible sets of frequency identifications, and with the TESS light curve, we can determine which is correct. Since the spectroscopic orbital frequency is unambiguously $\Omega = 9.1$

¹⁵ We exclude the object CG X-1 from this group. CG X-1 was formerly considered a candidate polar and remains identified as such in the VSX at the time of writing. However, Esposito et al. (2015) and Qiu et al. (2019) reclassified it as an extragalactic high-mass X-ray binary.

¹⁶ The final paragraph in Section 4.2 of Littlefield et al. (2019) discusses circumstantial evidence against this particular reidentification for CD Ind.

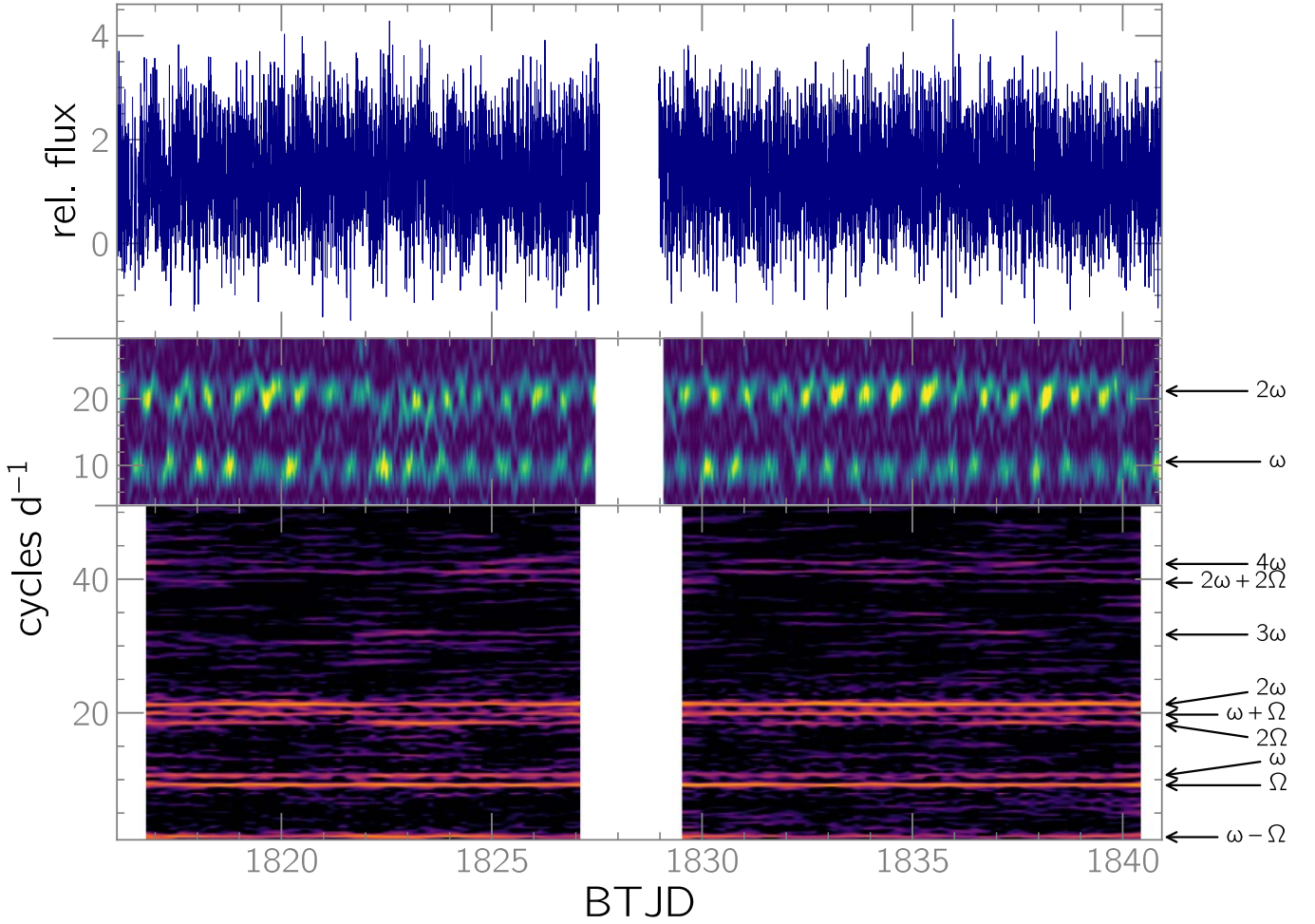


Figure 5. Top: the TESS light curve of Paloma. BTJD is defined as BJD $-2,457,000$. Middle: 2D power spectrum with a 0.25-day sliding window, with linear intensity scaling. Across the 0.7-day beat cycle, the light curve alternates between a single- and double-humped profile, causing power to shift cyclically between ω and 2ω . Bottom: 2D power spectrum with a 2-day sliding window and logarithmic scaling. The larger window size offers improved frequency resolution at the expense of completely concealing the changes evident in the middle panel.

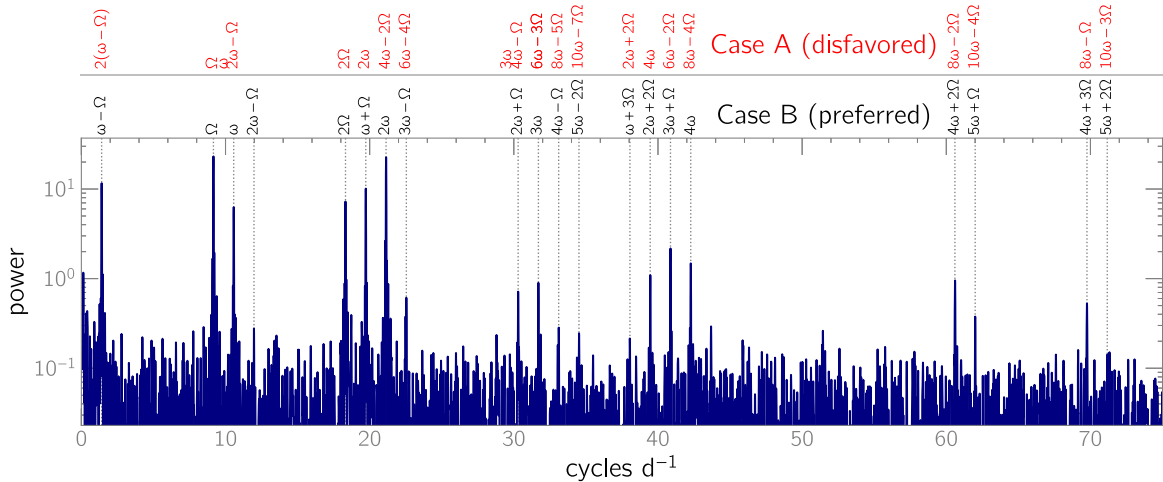


Figure 6. Lomb–Scargle power spectrum of the TESS light curve of Paloma, with the two sets of frequency identifications proposed by Schwarz et al. (2007). The usage of “Case A” and “Case B” matches that of Schwarz et al. (2007). For the Case A identifications, there would be no appreciable signal at either ω or $\omega - \Omega$. For reasons discussed in the text, we prefer the “Case B” identifications.

cycles day⁻¹ (Schwarz et al. 2007), there are only two plausible identifications of Paloma’s signal at 10.5 cycles day⁻¹: the $2\omega - \Omega$ sideband, or the spin frequency ω . Schwarz et al. (2007) refer to these two scenarios as Case A and Case B,

respectively. The X-ray study presented by Joshi et al. (2016) argued for Case B, and we concur.

In the Schwarz et al. (2007) Case A, the identification of the $2\omega - \Omega$ sideband would require the true spin frequency ω to be

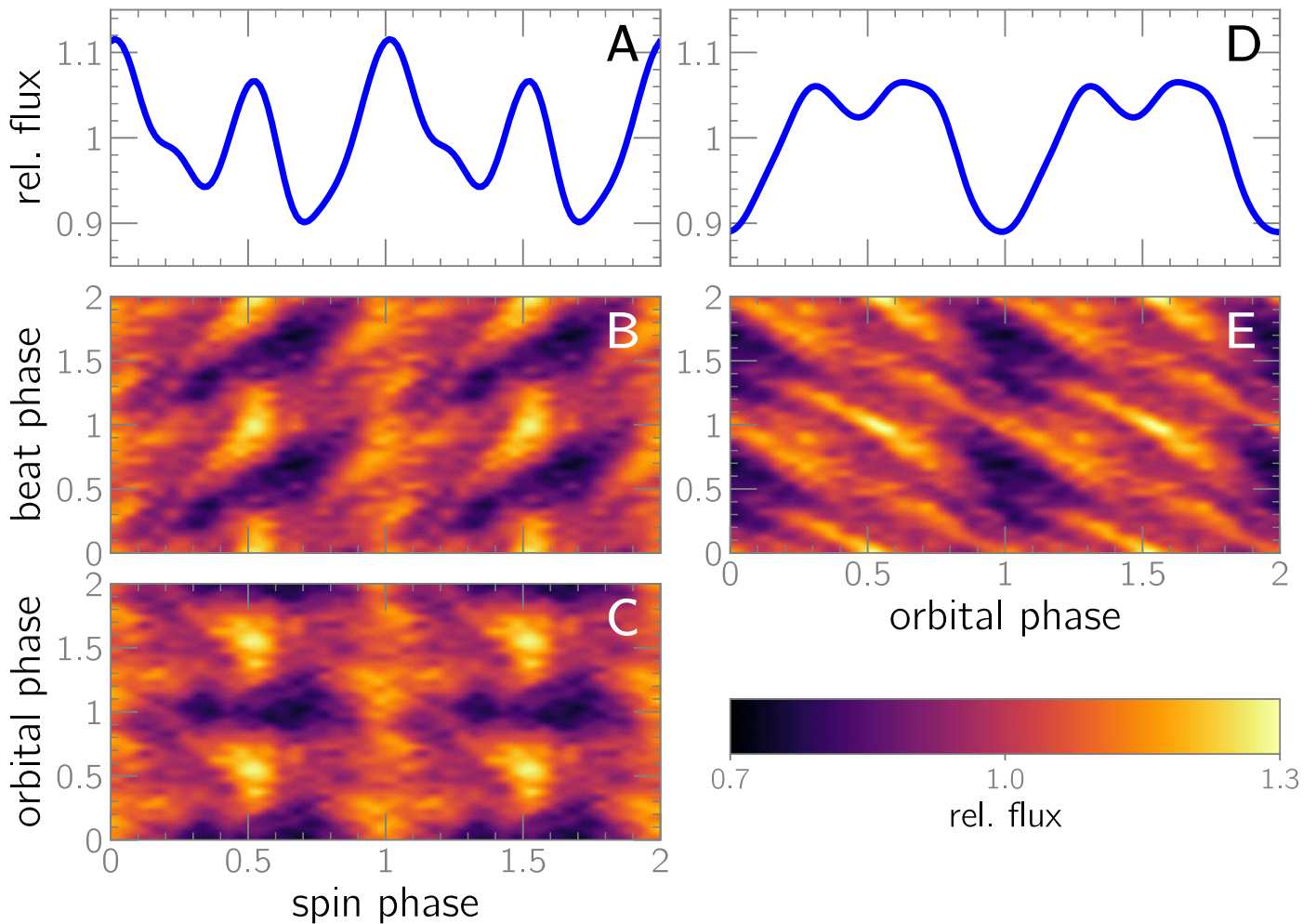


Figure 7. Interdependence of Paloma’s spin and orbital profiles across the beat cycle (relative to T_0 , $\text{beat[BJD]} = 2,458,836.1495$). Panels (a)–(c) share the same x -axis (spin phase relative to T_0 , $\text{spin[BJD]} = 2,458,836.9065$), while panels (d) and (e) show the orbital phase on a common x -axis. Panels (a) and (d) present six-harmonic Fourier-series representations of the average spin and orbital profiles across the entire TESS observation. Horizontal slices through panels (b) and (c) yield the spin profile that would be observed if the beat and orbital phases, respectively, could be held constant, and panel (c) shows that the secondary spin maximum disappears at inferior conjunction. Similarly, panel (e) shows the evolution of the orbital profile across the beat cycle. Panel (c) establishes that the spin profile changes significantly near inferior conjunction.

equidistant between $\Omega = 9.1 \text{ cycles day}^{-1}$ and $2\omega - \Omega = 10.5 \text{ cycles day}^{-1}$. Although there is a signal near this frequency in the Schwarz et al. (2007) power spectra, there is none in either the TESS or Joshi et al. (2016) power spectra. Case A further demands a beat frequency of $0.7 \text{ cycles day}^{-1}$. The TESS power spectrum shows no significant power at this frequency. Moreover, for Case A to be correct, all power at the fundamental spin and beat frequencies would need to be shifted into harmonics, a scenario that is unlikely.

Conversely, in the Schwarz et al. (2007) Case B identifications, the frequency at $10.5 \text{ cycles day}^{-1}$ is ω , resulting in a beat frequency $\omega - \Omega$ of $1.4 \text{ cycles day}^{-1}$. The TESS power spectrum contains a very strong signal at precisely that frequency. There would also be significant signals at ω and its next three harmonics—unlike Case A, where only the 2ω and 4ω harmonics would have significant power. While the Case B identifications would require there to be negligible power at $2\omega - \Omega$, the appearance of this frequency in power spectra depends on the orbital inclination and the colatitude of the accretion region; it is not expected to be universally present in diskless accretors (Wang et al. 2020).

We therefore agree with Joshi et al. (2016) that Case B from Schwarz et al. (2007), in which $\omega - \Omega = 1.4 \text{ cycles day}^{-1}$ and $\omega = 10.5 \text{ cycles day}^{-1}$, is the correct set of frequency identifications.

A remaining loose thread from this discussion is the nature of the signal detected by Schwarz et al. (2007) at $9.87 \text{ cycles day}^{-1}$, the putative spin frequency in their Case A. Schwarz et al. (2007) pointed out that in Case B this would be the first subharmonic of the $\omega + \Omega$ sideband—i.e., $9.87 \text{ cycles day}^{-1} = (\omega + \Omega)/2$. Subharmonics are not expected to be present in a Lomb–Scargle power spectrum like ours, but Schwarz et al. (2007) used the analysis-of-variance (AOV) algorithm to compute their power spectra. One property of AOV power spectra is that they can contain subharmonics of signals, and we agree with Schwarz et al. (2007) that this is a likely explanation for the signal at $9.87 \text{ cycles day}^{-1}$ in their AOV power spectrum.

4.2. The Orbital Phase Dependence of the Spin Pulse

The unbinned light curve of Paloma is rather noisy, but because the spin and orbital frequencies are known, we can phase-average the light curve to improve the signal-to-noise

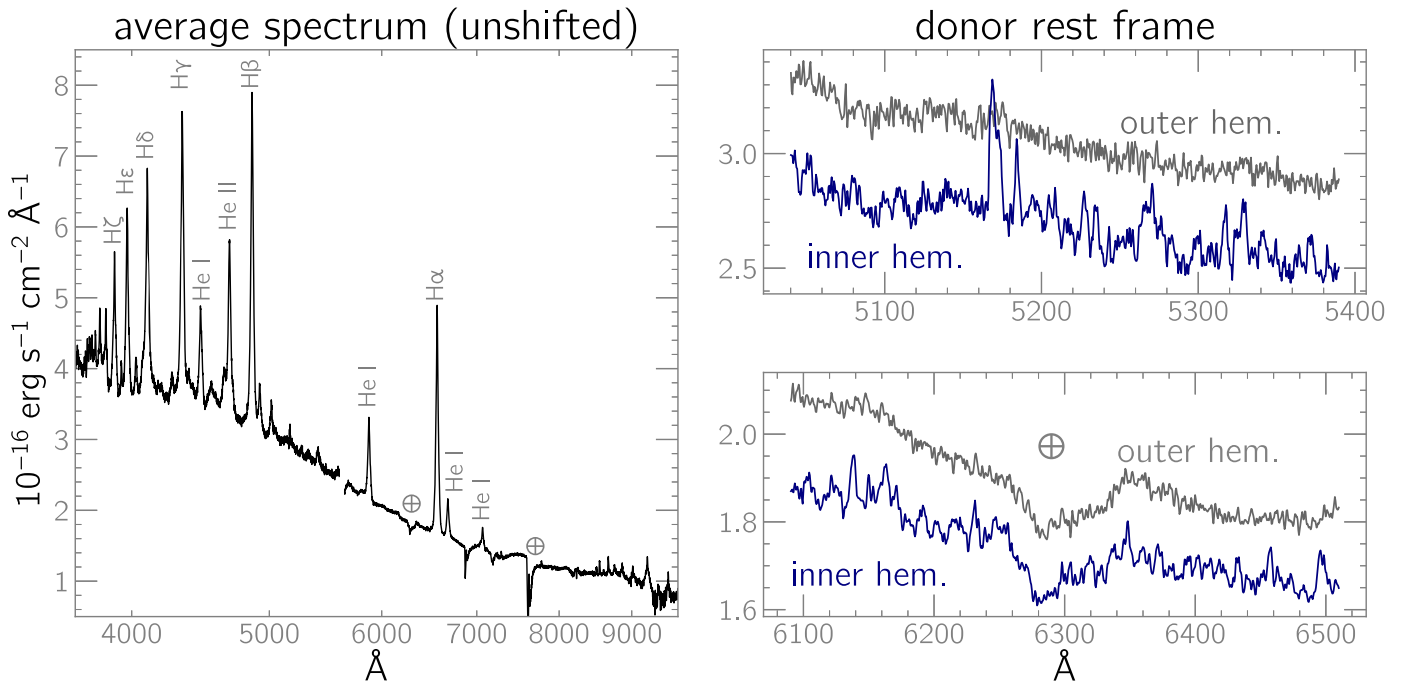


Figure 8. Left: average spectrum of Paloma, without any velocity shift applied. Telluric features have not been removed. Right panels: segments of the average spectra in the donor star’s rest frame, showing a forest of weak metal emission lines from the inner hemisphere. The velocity-corrected spectra are based on the measured semi-amplitudes of 220 and 310 km s⁻¹ for the secondary’s inner and outer hemispheres, respectively.

ratio. Figure 7 reveals the complex interplay between the spin and orbital profiles throughout the TESS observation. The spin profile shows two distinct maxima, separated in phase by 0.5 rotational cycles. Interestingly, the secondary maximum, which occurs at spin phase 0.5, is present for only part of the beat cycle and is not visible when it coincides with the secondary’s inferior conjunction (the epoch of which is measured in Section 4.3). In contrast, the primary spin maximum (spin phase 0.0) is present throughout the light curve and shows very little dependence on the orbital or spin phases. Because the amplitude of the secondary spin pulse is so strongly modulated across the beat cycle, we define a reference epoch (T_0 , beat [BJD] = 2,458,836.1495) such that the secondary maximum attains its maximum amplitude at beat phase 0.0, and we use this definition when phase-folding data in Figure 7.

While the orbital profile (Figure 7(e)) is not nearly as intricate as the spin profile, it shows a wide dip at inferior conjunction. The structure of this profile suggests that the secondary’s inner hemisphere contributes significantly to the TESS light curve and that the dip occurs when the inner hemisphere is mostly blocked by the secondary’s cool back side.

There are two scenarios that could account for the behavior in Figure 7: pole switching, and a grazing eclipse of one of the emitting regions. We shall consider the strengths and weaknesses of each hypothesis separately.

4.2.1. Scenario 1: Pole Switching

In the pole-switching scenario, accretion onto one of the poles ceases for half of the beat cycle, while the other pole accretes continuously. The preference for accretion onto one of the poles would require the magnetic-field topology to be more complex than a simple, centered dipole. One strength of this explanation is that it is consistent with the power-spectral evidence (both here and in Joshi et al. 2016) that Paloma is a

diskless IP. In the absence of a disk, one or more magnetic poles can be temporarily and periodically starved of a matter supply. Conversely, in a disk-fed IP, the inner rim of the disk provides a reservoir of material for both accretion regions, independent of the WD’s rotation.

4.2.2. Scenario 2: a Grazing Eclipse

An alternative explanation is that the spin pulse is intrinsically the same across the observations but is extrinsically altered by an eclipse. Figure 7 establishes that the pulse from the second pole disappears when it coincides with the secondary’s inferior conjunction. This phasing is exactly what is expected of a grazing eclipse by the donor star.

The chief difficulty with this scenario, however, is the absence of eclipses in the Joshi et al. (2016) X-ray observations, which covered a full beat cycle. X-rays in IPs are emitted from a post-shock region just above the WD’s photosphere, so an eclipse of the WD will produce sharp, energy-independent dips every orbital cycle. Thus, the nondetection of such a feature is very strong evidence that the WD itself is not eclipsed by the secondary. However, the eclipse interpretation of Figure 7 nevertheless remains tenable. This is because the optical spin pulse might be produced in extended accretion curtains away from the WD, as has been observed for, e.g., FO Aqr (Beardmore et al. 1998). If one of these curtains is blocked by the secondary at inferior conjunction, it could easily explain the disappearance of one of the maxima of the spin profile in Figure 7 without a corresponding eclipse at X-ray energies.

The available evidence does not offer an obvious answer as to which scenario (if either) is correct. However, it is difficult to dismiss as a coincidence the fact that one of the spin maxima disappears only when it is observed at inferior conjunction, and it is this factor that leads us to tentatively favor the eclipse interpretation. Spectroscopic observations of the eclipse-like

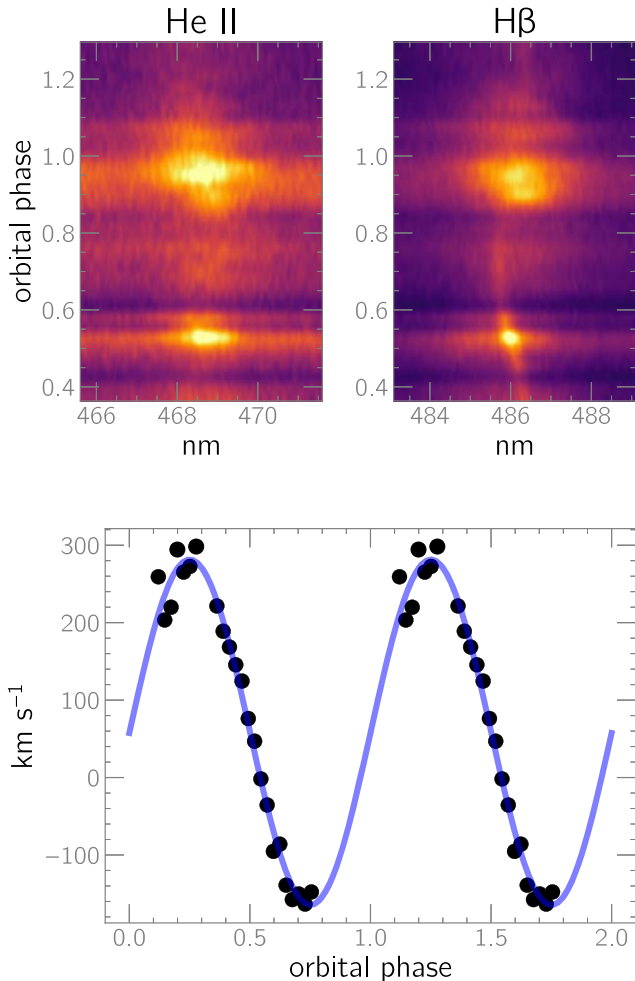


Figure 9. Top: continuum-subtracted, 2D spectra of He II $\lambda 4686$ and H β . There is no evidence of an eclipse at inferior conjunction. The two panels use different intensity cuts. Bottom: Radial-velocity curve of the Ca II triplet, showing a semi-amplitude of 220 km s^{-1} with a systemic velocity of 60 km s^{-1} . The blue-to-red crossing establishes the epoch of inferior conjunction. The Ca II line fluxes near the time of inferior conjunction have been excluded because they are very low. This suggests that the secondary’s inner hemisphere is occluded by the rest of the star near inferior conjunction, consistent with a moderate-to-high orbital inclination.

feature might offer a more definitive answer, as the eclipse of an accretion curtain should produce a concomitant weakening of the high-velocity components of the H and He emission lines.

4.3. Orbital Ephemeris from LBT Spectroscopy

The LBT spectra enable us to phase Paloma’s TESS light curve to the binary orbit because several features from the donor star are present. In particular, there is significant emission at the Ca II $\lambda\lambda 8498, 8542, 8662$ triplet from the secondary’s inner hemisphere, and the Na I $\lambda\lambda 8183, 8195$ absorption doublet is weakly present. In addition to the Ca II triplet, Paloma’s spectrum contains a large number of narrow, weak metal lines that are visible when the secondary’s irradiated inner hemisphere is viewed preferentially (Figure 8).

The Ca II emission and the Na I absorption move in phase with each other, and since the signal-to-noise ratio of the Ca II lines is significantly higher, we measure their motion to obtain

a radial-velocity curve (Figure 9). The blue-to-red crossing of the Ca II lines yields the time of the donor’s inferior conjunction, for which we provide an ephemeris of

$$T_{\text{conj}}[\text{BJD}] = 2458836.9131(2) + 0.10914(12) \times E. \quad (1)$$

Since the spectra were obtained during the TESS observation, the relative imprecision of the orbital period results in negligible phasing errors across the month-long TESS light curve.

Given the complexity of the LBT spectra, it is beyond the scope of this paper to analyze them comprehensively, and we will do so in a separate paper. However, an initial analysis of the spectra does not offer a clear-cut explanation of the variable secondary spin maximum discussed earlier. The observations were obtained between beat phases 0.98 and 1.12, which is outside the interval during which the secondary maximum vanishes at inferior conjunction (Figure 7). The spectra do provide evidence of a moderately high orbital inclination, as evidenced by the precipitous decline of the secondary’s metal emission lines from the inner hemisphere near inferior conjunction. This behavior, which is the reason for the lack of measured radial velocities for the Ca II triplet near inferior conjunction in Figure 9, is likely the result of the secondary’s irradiated inner hemisphere being hidden by its back side. However, there is no evidence of an eclipse of the accretion flow in either the He II or H β lines in Figure 9.

4.4. The Spin-period Derivative of Paloma

With a sufficiently long (\sim decades) observational baseline, we would expect Paloma to show a spin-period derivative (\dot{P}), as has been observed in all APs with such baselines (for a recent summary, see Table 1 in Myers et al. 2017). These systems have a characteristic synchronization time-scale $\tau = |(P_{\text{orb}} - P_{\text{spin}})|/\dot{P}$.

We measure a spin period of 0.09460(10) days at Julian year epoch 2019.94, compared to a period of 0.094622(3) days in observations between 1992 and 2002 (Schwarz et al. 2007). Because the Schwarz et al. (2007) value falls within our 1σ uncertainty for the spin period, we do not detect evidence of a statistically significant \dot{P} . This nondetection is subject to an important caveat: the Schwarz et al. (2007) period suffers from a cycle-count ambiguity.

Although the nondetection of \dot{P} is disappointing, it is not unexpected, given the relatively large uncertainty of the TESS spin period. The maximum observed \dot{P} in FO Aqr, an IP famous for its rapidly varying spin period, is $|\dot{P}| = 8 \times 10^{-10}$ (Littlefield et al. 2020). If the Schwarz et al. (2007) period were either increasing or decreasing at that rate, the change in period would be indiscernible a quarter century later at the precision of the TESS spin period. Without long-term, highly precise measurements of the spin period, it will be challenging to convincingly detect \dot{P} in Paloma.

5. Conclusion

We have used a long-cadence K2 light curve to show that J0846 is a new AP with a significantly longer orbital period than any other AP. Our analysis of the TESS light curve of another nearly synchronous mCV, Paloma, eliminates the long-standing ambiguity surrounding the proper identification of its spin frequency. Both targets warrant long-term monitoring so that their spin-period derivatives can be measured.

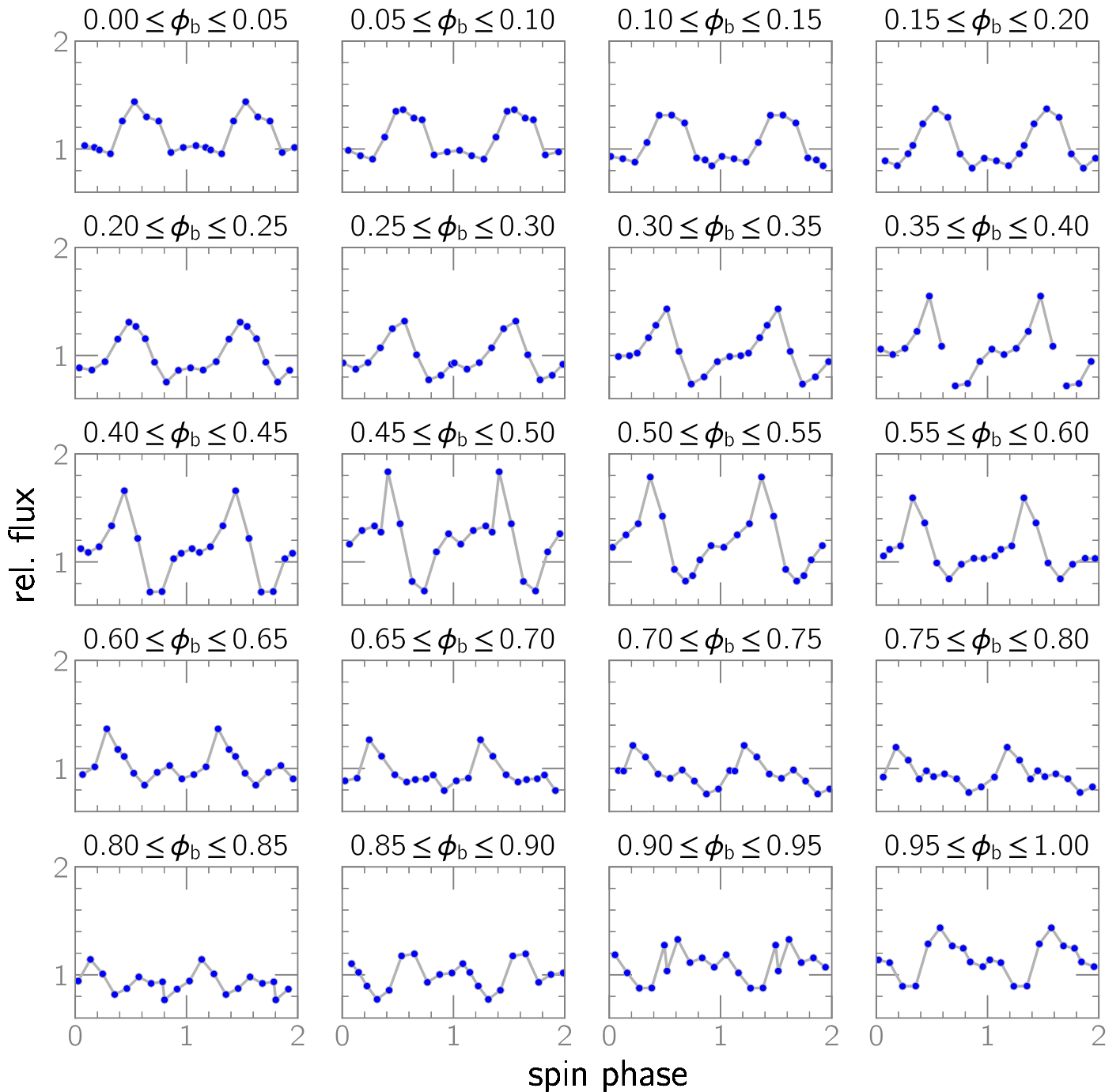


Figure 10. Binned spin profiles of J0846 in 20 nonoverlapping portions of the 6.7-day beat cycle. The top of each panel indicates which beat phases were used to construct each spin profile. The data are repeated along the x -axis for clarity. The pole near spin phase 0.5 has an associated photometric maximum for most of the beat cycle, but it becomes indistinct near beat phase 0.8. Error bars are too small to be visible at this scale.

We thank the anonymous referee for their helpful review of this manuscript.

P.S., D.H., and C.L. acknowledge support from NSF grant AST-1514737. M.R.K. acknowledges support from the Irish Research Council in the form of a Government of Ireland Postdoctoral Fellowship (GOIPD/2021/670: invisible Monsters). P.G. and C.L. acknowledge support from NASA grants 80NSSC19K1704 and 80NSSC22K0183. K.I. acknowledges support from Polish National Science Center grant 2021/40/C/ST9/00186. P.A.M. acknowledges support from Picture Rocks Observatory. This research has made use of the

International Variable Star Index (VSX) database, operated at AAVSO, Cambridge, Massachusetts, USA.

Facility: Large Binocular Telescope.

Software: *astropy* (Astropy Collaboration et al. 2013), *lightkurve* (Lightkurve Collaboration et al. 2018).

Appendix

Beat-phase-resolved Spin Profiles of J0846 and Paloma

The K2 and TESS data showcase the gradual evolution of the spin profiles of both J0846 and Paloma across their

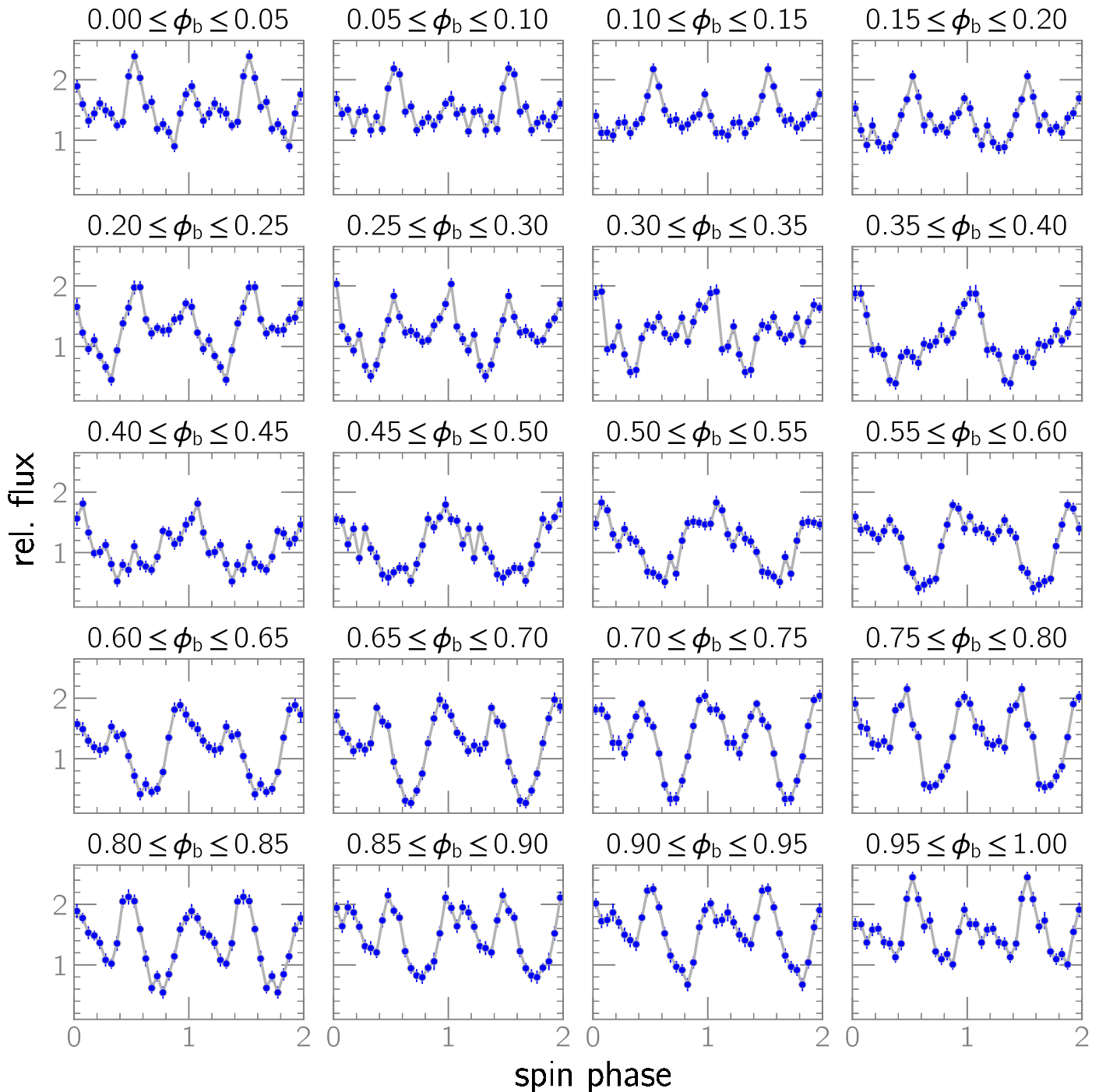


Figure 11. Evolution of Paloma’s spin profile across the beat cycle. Beat phase 0.0 occurs when the primary spin maximum coincides with inferior conjunction of the secondary star (i.e., when the spin and orbital phases are both 0.0).

respective beat cycles. Figures 4 and 7 used 2D light curves to illustrate this behavior.

Here we present 1D light curves of the spin profiles of both J0846 and Paloma to enable a more careful inspection than is possible in their 2D counterparts. Because the resulting figures are awkwardly large, we present them separately from the main text in Figures 10 and 11 for J0846 and Paloma, respectively.

ORCID iDs

Colin Littlefield <https://orcid.org/0000-0001-7746-5795>

Peter Garnavich <https://orcid.org/0000-0003-4069-2817>
 Paula Szkody <https://orcid.org/0000-0003-4373-7777>
 Paul A. Mason <https://orcid.org/0000-0002-5897-3038>
 Krystian Ilkiewicz <https://orcid.org/0000-0002-4005-5095>
 Mark R. Kennedy <https://orcid.org/0000-0001-6894-6044>
 Saul A. Rappaport <https://orcid.org/0000-0003-3182-5569>
 Rahul Jayaraman <https://orcid.org/0000-0002-7778-3117>

References

- Astropy Collaboration, Robitaille, T. P., Tollerud, E. J., et al. 2013, *A&A*, **558**, A33
- Bailer-Jones, C. A. L., Rybizki, J., Foesneau, M., Demleitner, M., & Andrae, R. 2021, *AJ*, **161**, 147
- Beardmore, A. P., Mukai, K., Norton, A. J., Osborne, J. P., & Hellier, C. 1998, *MNRAS*, **297**, 337
- Bellm, E. C., Kulkarni, S. R., Graham, M. J., et al. 2019, *PASP*, **131**, 018002
- Beuermann, K., Burwitz, V., Reinsch, K., Schwöpe, A., & Thomas, H.-C. 2021, *A&A*, **645**, A56
- Bochanski, J. J., West, A. A., Hawley, S. L., & Covey, K. R. 2007, *AJ*, **133**, 531
- Chanmugam, G., & Ray, A. 1984, *ApJ*, **285**, 252
- Cropper, M. 1990, *SSRv*, **54**, 195
- Drake, A. J., Graham, M. J., Djorgovski, S. G., et al. 2014, *ApJS*, **213**, 9
- Esposito, P., Israel, G. L., Milisavljevic, D., et al. 2015, *MNRAS*, **452**, 1112
- Gaia Collaboration, Brown, A. G. A., Vallenari, A., et al. 2021, *A&A*, **649**, A1
- Gaia Collaboration, Prusti, T., de Bruijne, J. H. J., et al. 2016, *A&A*, **595**, A1
- Geckeler, R. D., & Staubert, R. 1997, *A&A*, **325**, 1070
- Hakala, P., Ramsay, G., Potter, S. B., et al. 2019, *MNRAS*, **486**, 2549
- Halpern, J. P. 2022, *ApJ*, **934**, 123
- Halpern, J. P., Bogdanov, S., & Thorstensen, J. R. 2017, *ApJ*, **838**, 124
- Hill, K. L., Littlefield, C., Garnavich, P., et al. 2022, *AJ*, **163**, 246
- Joshi, A., Pandey, J. C., Singh, K. P., & Agrawal, P. C. 2016, *ApJ*, **830**, 56
- King, A. R. 1993, *MNRAS*, **261**, 144
- King, A. R., & Lasota, J.-P. 1991, *ApJ*, **378**, 674
- King, A. R., & Wynn, G. A. 1999, *MNRAS*, **310**, 203
- Lightkurve Collaboration, Cardoso, J. V. d., Hedges, C., et al. 2018, *Lightkurve: Kepler and TESS time series analysis in Python*, Astrophysics Source Code Library, ascl:1812.013
- Littlefield, C., Garnavich, P., Kennedy, M. R., et al. 2020, *ApJ*, **896**, 116
- Littlefield, C., Garnavich, P., Mukai, K., et al. 2019, *ApJ*, **881**, 141
- Littlefield, C., Mukai, K., Mumme, R., et al. 2015, *MNRAS*, **449**, 3107
- Littlefield, C., Scaringi, S., Garnavich, P., et al. 2021, *AJ*, **162**, 49
- Lomb, N. R. 1976, *Ap&SS*, **39**, 447
- Mason, P. A., Andronov, I. L., Kolesnikov, S. V., Pavlenko, E. P., & Shakovskoy, M. 1995, in ASP Conf. Ser. 85, *Magnetic Cataclysmic Variables*, ed. D. A. H. Buckley & B. Warner (San Francisco, CA: ASP), 496
- Mason, P. A., Liebert, J., & Schmidt, G. D. 1989, *ApJ*, **346**, 941
- Mason, P. A., Morales, J. F., Littlefield, C., et al. 2020, *AdSpR*, **66**, 1123
- Mason, P. A., Ramsay, G., Andronov, I., et al. 1998, *MNRAS*, **295**, 511
- Myers, G., Patterson, J., Miguel, E. d., et al. 2017, *PASP*, **129**, 044204
- Patterson, J. 1994, *PASP*, **106**, 209
- Pavlenko, E., Andreev, M., Babina, Y., & Malanushenko, V. 2013, in ASP Conf. Ser. 469, *18th European White Dwarf Workshop*, ed. J. Krzesiński et al. (San Francisco, CA: ASP), 343
- Pavlenko, E. P., Mason, P. A., Sosnovskij, A. A., et al. 2018, *MNRAS*, **479**, 341
- Pogge, R. W., Atwood, B., Brewer, D. F., et al. 2010, *Proc. SPIE*, **7735**, 77350A
- Qiu, Y., Soria, R., Wang, S., et al. 2019, *ApJ*, **877**, 57
- Rawat, N., Pandey, J. C., & Joshi, A. 2021, *ApJ*, **912**, 78
- Rawat, N., Pandey, J. C., Joshi, A., Scaringi, S., & Yadava, U. 2022, *MNRAS*, **517**, 1667
- Scargle, J. D. 1982, *ApJ*, **263**, 835
- Schmidt, G. D., & Stockman, H. S. 1991, *ApJ*, **371**, 749
- Schwarz, R., Schwöpe, A. D., Staude, A., et al. 2007, *A&A*, **473**, 511
- Stockman, H. S., Schmidt, G. D., & Lamb, D. Q. 1988, *ApJ*, **332**, 282
- Szkody, P., Henden, A., Agueros, M., et al. 2006, *AJ*, **131**, 973
- Tovmassian, G., Gonzalez-Buitrago, D., Thorstensen, J., et al. 2017, *A&A*, **608**, A36
- Wang, Q., Qian, S., Han, Z., et al. 2020, *ApJ*, **892**, 38
- Wynn, G. A., & King, A. R. 1992, *MNRAS*, **255**, 83
- Zhilkin, A. G., Bisikalo, D. V., & Mason, P. A. 2012, *ARRep*, **56**, 257
- Zhilkin, A. G., Bisikalo, D. V., & Mason, P. A. 2016, in AIP Conf. Ser. 1714, *Space Plasma Physics* (Melville, NY: AIP), 020002